Res Chem Intermed (2018) 44:3061–3079
https://doi.org/10.1007/s11164-018-3293-4

Enhanced photocatalytic degradation for organic pollutants by a novel m-Bi_2O_4/$Bi_2O_2CO_3$ photocatalyst under visible light

Junxiu Wang[1] · Kuan Chen[1] · Yi Shen[1] · Xi Wang[1] · Yongfu Guo[1] · Xiaoji Zhou[1] · Renbi Bai[1]

Received: 4 October 2017 / Accepted: 17 January 2018 / Published online: 25 January 2018

Abstract To heighten the absorption to visible light and improve photocatalytic degradation to organic pollutants, a novel photocatalyst of m-Bi_2O_4/$Bi_2O_2CO_3$ was constructed through a facile hydrothermal method. The crystal structure, optical properties, morphology, composition and photocatalytic ability of the photocatalysts were characterized via X-ray diffraction, Fourier transform infrared spectroscopy, ultraviolet–visible diffuse reflectance spectroscopy, field emission scanning electron microscopy, energy dispersive spectroscopy, transmission electron microscope (TEM), high resolution TEM, selected-area electron diffraction and X-ray photoelectron spectroscopy technologies. The as-prepared photocatalysts could efficiently degrade rhodamine B and mixed dye under visible light. The removal rate was up to 95.3% within 50 min. The results demonstrated that m-Bi_2O_4/$Bi_2O_2CO_3$ photocatalysts showed outstanding photocatalytic degradation ability compared to the single photocatalyst with the narrow band gap. In addition, photocurrent response tests certified that the heterostructure of the photocatalysts effectively accelerated the separation and migration of photo-induced electrons and holes. Active species trapping experiments indicated that holes (h^+) and superoxide radical ($\bullet O_2^-$) were major species rather than hydroxyl radicals (•OH) during the degradation process of organics. According to the test results, a probable photocatalytic mechanism was proposed.

Electronic supplementary material The online version of this article (https://doi.org/10.1007/s11164-018-3293-4) contains supplementary material, which is available to authorized users.

✉ Yongfu Guo
yongfuguo@163.com

✉ Renbi Bai
ceebairb@live.com

[1] Center for Separation and Purification Materials and Technologies, Suzhou University of Science and Technology, Suzhou 215009, Jiangsu, People's Republic of China

This work provided a new and efficient photocatalyst for environmental remediation and water treatment.

Graphical Abstract

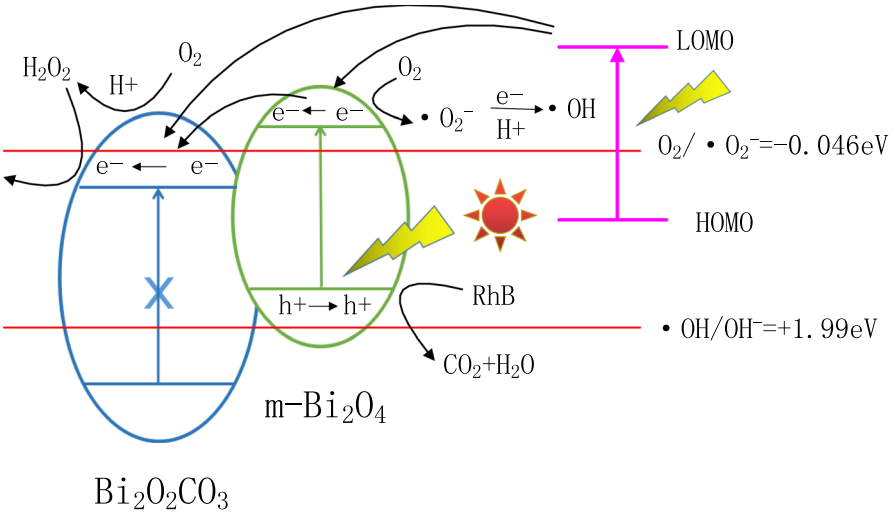

Keywords Photocatalysis · Degradation · Organic pollutant · Photocatalyst · Mechanism

Introduction

Dye wastewater containing intractable organic compounds is generated mainly from paper industries, textile dyeing and dye intermediate industries [1]. The composition of dye wastewater is normally complex and contains a lot of salt and harmful substances. It has some features including high chemical oxygen demand (COD_{cr}), deep colour and poor biodegradability. The traditional methods of dealing with dye wastewater by absorption, chemical reaction or biological degradation are difficult to use to remove dye molecules from water due to their complex nature.

Fortunately, there, in recent years, has been a promising technology to handle the problem. Photocatalysis can utilize sunlight as an energy source to effectively degrade organic pollutants. Since it has many advantages, such as an environmental friendly nature, low cost, nontoxicity and feasible operation under ambient conditions, etc., photocatalytic technology has gotten much more attraction.

Up to now, the general mechanism of photocatalysis has been suggested and is becoming mature.

Normally, when a semiconductor is illuminated by light with high enough energy, it will produce electron (e^-) and hole (h^+) pairs. Among these photo-generated carriers, some move so slowly that they will recombine in the internal part,

and the energy is lost in the form of heat. Others migrate to the surface of the photocatalyst and produce positive and negative charges at the same time, similar to the anode and cathode of an electrolytic cell. The materials in the system, such as organics, O_2, H^+ and so on, act as electron acceptors or donors. Photocatalytic reaction occurs while electrons and holes react with certain substances, including hydroxyl radicals (•OH), superoxide radical ($•O_2^-$), •OOH, etc. When the value of the valence band (VB) in a photocatalyst is more positive than that in the organic oxidation potential, the oxidation reaction takes place [2].

Titanium dioxide (TiO_2) is a common photocatalyst; nevertheless, the disadvantages limit its application. TiO_2 has a large band gap (~ 3.2 eV) and only responds to UV light which occupies approximately 4–5% of sunlight with low quantum efficiency [3, 4]. In addition, the rapid recombination of photo-generated e^- and h^+ reduces the photocatalytic activity [5, 6].

Nowadays, bismuth-based semiconductors, like $BiVO_4$ [7], Bi_2WO_6 [8], Bi_2O_3 [9, 10] and BiOBr [11] have been getting much attention, and their VBs consist of the hybridization of O *2p* and Bi *6 s* orbits [12]. Among these semiconductors, $Bi_2O_2CO_3$ has a typical Sillén structure firstly reported by Grice's group. In the structure of $Bi_2O_2CO_3$, $(Bi_2O_2)^{2+}$ and $[CO_3]^{2-}$ alternate with the $[CO_3]^{2-}$ group orthogonal to $(Bi_2O_2)^{2+}$ layer plane, as shown in Fig. 1. Owing to the internal electronic field, these layered photocatalysts are able to separate photo-generated carriers selectively and migrate them quickly [13, 14]. It can be clearly seen the segregated "standing-on-end" carbonate layer in Fig. 1 [15, 16].

However, $Bi_2O_2CO_3$ also has shortcomings that needed to be improved. That some cationic clusters are grafted on the surface of $Bi_2O_2CO_3$ is becoming a new strategy, which can enable effectively promoting carrier separation through the interfacial charge transfer [17–19]. Some researchers utilized magnetism to increase its performance. Hu et al. [16] synthesized a visible-light-driven photocatalyst of $Bi_2O_2CO_3$@Fe_2O_3 and Zhu et al. [20] demonstrated Fe_3O_4/$Bi_2O_2CO_3$ by the hydrothermal method. These could be applied in recyclable degradation.

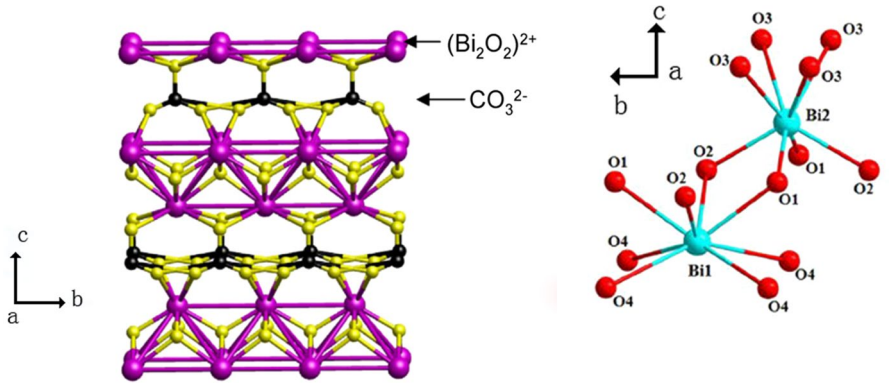

Fig. 1 Crystal structure of $Bi_2O_2CO_3$

Heterostructured photocatalysts not only improve the adsorption to visible light, but also efficiently reduce the recombination of photo-generated charge carriers and enhance photocatalytic activity [21]. For example, $Bi_2O_2CO_3$/BiOCl [22], $Bi_2O_2CO_3/Bi_2S_3$ [23], AgI/$Bi_2O_2CO_3$ [24] and g-C_3N_4/$Bi_2O_2CO_3$ [25], etc., exhibited remarkable degradation ability. In the composite photocatalysts, the moving direction of photo-induced carriers is changed; and the separated efficiency is also improved, leading to a significant photocatalytic activity [26]. However, these photocatalysts still have some defects, such as violent reaction conditions, complex operation, large band gap and slow degradation rate, etc.

Recently, a novel photocatalyst of monoclinic dibismuth tetraoxide (m-Bi_2O_4) was constructed, which can work under the condition of visible light. The Bi in m-Bi_2O_4 is composed of mixed valent states of Bi(III) and Bi(V). The m-Bi_2O_4 photocatalyst possesses a narrow band gap (~ 2.0 eV) and can absorb wavelengths up to 620 nm [27], producing a good degradation activity for organic pollutants under visible light [27]. Its characteristics attract much attention. Xia et al. successfully synthetized Bi_2O_4/Fe_3O_4 hybrid nanocomposite through an in situ growth method and applied it to degrade ibuprofen. The results showed a better photocatalytic activity [28]. They also constructed a novel Z-scheme g-C_3N_4/m-Bi_2O_4 photocatalyst, which could inactivate *E. coli* K-12 within 1.5 h under visible light [29].

Given the advantages of m-Bi_2O_4 and the researches of $Bi_2O_2CO_3$, we synthetized m-$Bi_2O_4/Bi_2O_2CO_3$ photocatalyst by a hydrothermal method to narrow the band gap and speed up the separation of e^- and h^+. Meanwhile, the photocatalytic activities for rhodamine B (RhB) and mixed dyes were investigated under visible light. Moreover, the degradation mechanism of a m-$Bi_2O_4/Bi_2O_2CO_3$ heterojunction photocatalyst was also proposed.

Experimental

Materials and reagents

All of the purchased reagents were in analytical grade. Bismuth nitrate pentahydrate ($Bi(NO_3)_3{\cdot}5H_2O$), sodium carbonate (Na_2CO_3), rhodamine B (RhB) and isopropanol (IPA) were purchased from Macklin Reagents (Shanghai) Co., Ltd. Cetyltrimethyl ammonium bromide (CTAB), sodium bismuthate hydrate ($NaBiO_3{\cdot}2H_2O$), sodium oxalate ($Na_2C_2O_4$) and 4-hydroxyl-2, 2, 6, 6-tetramethylpiperidinyloxy (TEMPOL) were purchased from Aladdin Reagents (Shanghai).

Synthesis of $Bi_2O_2CO_3$ photocatalyst

$Bi_2O_2CO_3$ (BOC) was prepared based on the reported works [30, 31]. Typically, 9.7 g $Bi(NO_3)_3{\cdot}5H_2O$ was dissolved in 40 mL dilute nitric acid (1 mol/L) and then treated by ultrasound for 20 min to get a clarified solution A. The nitric acid avoided the hydrolysis of Bi^{3+}. Simultaneously, 2.0 g CTAB and 16.9 g Na_2CO_3 were dissolved in 180 mL ultrapure water to obtain solution B. Then, solution A was put

dropwise into B and stirred constantly. White precipitate in solution A would be formed immediately. After continuously stirred for 30 min, the resulted precipitate was filtrated and washed several times with absolute alcohol and ultrapure water. Ultimately, as-synthesized BOC sample was dried at 333 K for overnight.

Synthesis of m-Bi_2O_4/$Bi_2O_2CO_3$ photocatalyst

Heterostructured m-Bi_2O_4/$Bi_2O_2CO_3$ photocatalyst was prepared by a convenient one-pot hydrothermal method. Typically, 1.530 g BOC was dissolved into 90 mL ultrapure water with ultrasound applied. Then, a certain amount of $NaBiO_3{\cdot}2H_2O$ was dissolved into the above solution with vigorous magnetic stirring for 1 h at room temperature. The obtained uniform suspension was placed into a 150 mL Teflon autoclave and heated to 433 K for 12 h. After cooling down, the resulting precipitate was collected by centrifugation and then washed for three times. Finally, the product was dried at 333 K overnight. The obtained samples with different amounts of $NaBiO_3{\cdot}2H_2O$ were called X–B/BOC, where X referred to the molar ratio of m-Bi_2O_4 and $Bi_2O_2CO_3$ in theoretical calculations. Thence, these photocatalysts were named as 3-B/BOC, 6-B/BOC and 8-B/BOC based on various molar ratios.

Analytical methods

The purity and structure of as-synthesized materials were characterized by powder X-ray diffraction (XRD). Field emission transmission electron microscopy (TEM) and field emission scanning electron microscopy (FE-SEM) equipped with an energy dispersive X-ray spectroscopy detector (EDS) were used to detect the morphology and elemental content.

The valence states and composition were conducted by X-ray photoelectron spectroscopy (XPS). A Fourier transform infrared absorption spectrometer (FT-IR) was used to detect the functional groups. UV–vis diffuse reflectance spectrum (DRS) was obtained via an UV–vis–NIR Spectrophotometer. The above instruments were the same as previous reports [32, 33]. A photocurrent test was executed using a CHI-660E electrochemical station equipped with a standard three-electrode. A Xenon lamp (PLS-SEX300C, 300W) equipped with a cut-off filter ($\lambda > 420$ nm) was selected as the visible light source and the illuminance was 5000 Lux.

Evaluation of catalyst performance

The performance of above photocatalysts was evaluated through degrading RhB dye with a visible light instrument (CEL-HXF-300W).

The progress of photocatalytic degradation under visible light was made as follows: In each experiment, a certain amount of photocatalysts (25–75 mg) was dispersed into 100 mL RhB solution (5–20 mg/L, typically 10 mg/L). The light source was set at a distance of 14 cm from the liquid level. Before irradiation, the RhB solution was magnetically stirred in the dark for 1 h to ensure an adsorption–desorption equilibrium. During the process of irradiation, about 5 mL of reaction solution

was withdrawn at a given time interval and centrifuged to remove photocatalysts, and then analysed via the UV–vis spectrometer at 554 nm to determine the remaining concentration of pollutants after degradation.

The degradation ratio (η, %) was calculated based on the concentration (C_0, mg/L) of RhB after adsorption–desorption equilibrium and the concentration (C_t, mg/L) of RhB at any time t (min) during the process of photodegradation.

In order to estimate the practicality of the samples, mixed dyes including MO, RhB and MB were used as pollutants, and the mixed concentration was 10 mg/L (mass ratio of MO: RhB: MB = 1: 1: 1). The results of the degradation were characterized by absorption spectroscopy.

Active species trapping experiments

To further understand the probable mechanism of photocatalytic degradation and investigate the active species during the process, trapping experiments were conducted. Generally, active species include holes (h^+), the superoxide radical ($\bullet O_2^-$) and hydroxyl radicals ($\bullet$OH). In the test, IPA, $Na_2C_2O_4$ and TEMPOL were utilized as the scavengers for $\bullet$OH, h^+ and $\bullet O_2^-$, respectively. Different scavengers were added into the RhB solution and other conditions were the same as in the degradation experiments.

Results and discussion

Characterization of photocatalysts

XRD

The crystalline phase and purity were investigated by XRD, and the diffraction peaks are presented in Fig. 2.

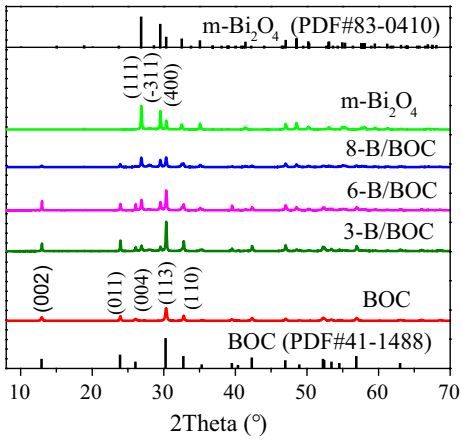

Fig. 2 XRD patterns of m-Bi_2O_4, m-Bi_2O_4/$Bi_2O_2CO_3$ and BOC

The diffraction peaks of BOC correspond to the tetragonal phase $Bi_2O_2CO_3$ (JPCDS card No. 41-1488, lattice constants: a = 3.865 Å, b = 3.865 Å, c = 13.675 Å) [34, 35]. The narrow peaks indicated high crystallinity and larger grain size of products. This indicates that the as-prepared samples exhibited excellent crystalline and purity. The main characteristic peaks of BOC samples at 12.91°, 23.90°, 26.08°, 30.32° and 32.79° corresponded to the crystal faces of (002), (011), (004), (013) and (110), respectively [36–38].

Compared to other diffraction peaks, the remarkable intensity of the (113) plane was attributed to the orientation bias of the crystallographic plane [39]. Pure m-Bi_2O_4 exhibited identical diffraction peaks similar to the monoclinic phase of Bi_2O_4 (JPCDS card No. 83-0410). The as-synthesized bismuth oxide can be seen as a composites with both Bi(III) and Bi(V) [27, 28]. Four characteristic peaks at 2θ of 26.86°, 29.52°, 30.36° and 32.51° could be indexed to (111), (-311), (400) and (-202) planes. While the amount of $NaBiO_3{\cdot}2H_2O$ was increased during the process of hydrothermal synthesis, the intensities of peaks of different samples at (111) and (-311) planes were enhanced and others were contrary, which meant a preferential growth of the crystallographic plane. For all of the m-Bi_2O_4/$Bi_2O_2CO_3$ nanocomposites, the diffraction peaks of both m-Bi_2O_4 and BOC phases were presented and no other impure peaks were detected.

FT-IR

In order to identify the chemical composition and analyse the chemical bond of as-prepared catalysts, FT-IR measurement was executed. The results are displayed in Fig. 3. As for BOC, the range of absorption peaks was between 500 and 2000 cm^{-1}. Two bands at about 3448 and 1637 cm^{-1} corresponded to the stretching and deformation vibration of an O–H group in physisorbed and/or chemisorbed H_2O [40, 41]. The peak at 546 cm^{-1} could be attributed to a Bi–O bond.

There were three kinds of "free" vibration modes of carbonate ions. Firstly, the band at 1070 cm^{-1} was assigned to the symmetric stretching mode ν_1 Secondly, the band at 846 cm^{-1} corresponded to the out-of-plane bending mode ν_2 in CO_3^{2-}. Strong peaks at 1392 and 1468 cm^{-1} were derived from the corresponding

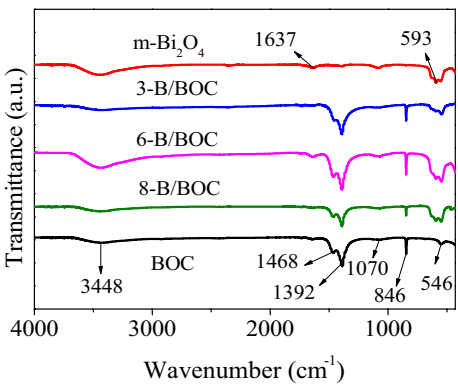

Fig. 3 FT-IR spectra of m-Bi_2O_4, BOC, 3-B/BOC, 6-B/BOC and 8-B/BOC samples

anti-symmetric vibration mode ν_3 [42–44]. No other impure peaks including NO_3^- were discovered. In the m-Bi_2O_4 spectrum, the band at 593 cm^{-1} was attributed to stretching vibrations of the Bi–O bond [45].

Comparing these spectra, it can be seen that with the increase of m-Bi_2O_4 content, the peak intensities of Bi–O bonds were enhanced while the band at 1392 cm^{-1} was reduced. Hence, FT-IR spectra together with XRD results demonstrated that the m-Bi_2O_4/$Bi_2O_2CO_3$ photocatalyst was successfully obtained.

Morphology characterization

The general morphologies of five catalysts were in-depth detected by SEM in Fig. 4.

The m-Bi_2O_4 sample was an irregular rod-like structure, and the length was approximately 1 μm, while the BOC consisted of some pill-like nanosheets with thickness of about 80 nm, as shown in Fig. 4a, b. The structures of other complexes are shown in Fig. 4c–e.

The EDS spectrum of 6-B/BOC samples illustrated the existence of Bi, O and C elements. The microstructure of crystal is presented in Fig. 4g–h by TEM and HR-TEM. The HR-TEM figure shows that the lattice fringes of 0.372 and 0.342 nm corresponded with the lattice planes (110) and (004) of BOC and the lattice spacing of 0.332 and 0.294 nm were ascribed to (111) and (400) crystal faces of m-Bi_2O_4.

The selected-area electron diffraction (SAED) is presented in Fig. 4i. The arranged regular highlights implied that the composite was a single crystalline structure. These figures led to the conclusion that the m-Bi_2O_4/$Bi_2O_2CO_3$ photocatalyst was successfully synthetized.

XPS analysis

The valent states and chemical composition of 6-B/BOC samples were further conducted by XPS measurement. As indicated in Fig. 5, the XPS survey spectra displayed that the composite contained only Bi, O and C elements. The asymmetric peak for O 1 *s* could be deconvoluted into three peaks at 528.9, 530.1 and 530.6 eV. The peak at 528.9 eV corresponded to the lattice oxygen in the Bi–O bond. The high binding energies at 530.1 and 530.6 eV were ascribed to the chemisorbed and physisorbed oxygen on the surface of the photocatalyst, respectively [46–48].

The two high-resolution peaks of Bi 4*f* corresponded to the positions of Bi $4f_{5/2}$ and Bi $4f_{7/2}$. The peak of Bi $4f_{5/2}$ was resolved into one bimodal peak at 164.1 and 163.4 eV. And the Bi $4f_{7/2}$ peak was deconvoluted into other bimodal peaks at 158.2 and 158.9 eV, which should be assigned to Bi(III) and Bi(V) on the basis of previous researches [28, 49]. The C 1 *s* XPS peak was two asymmetrical peaks, indicating that the distinguishable models of C existed simultaneously in the composite. The peak at 284.6 eV was adventitious carbon species from XPS measurement and other fitted peaks at 286.7 and 288.2 eV were assigned to an oxygen-bearing bond and a carbonate ion, separately [41]. Combined with the previous performance analysis, the results implied that the m-Bi_2O_4/$Bi_2O_2CO_3$ photocatalyst was successfully synthesized.

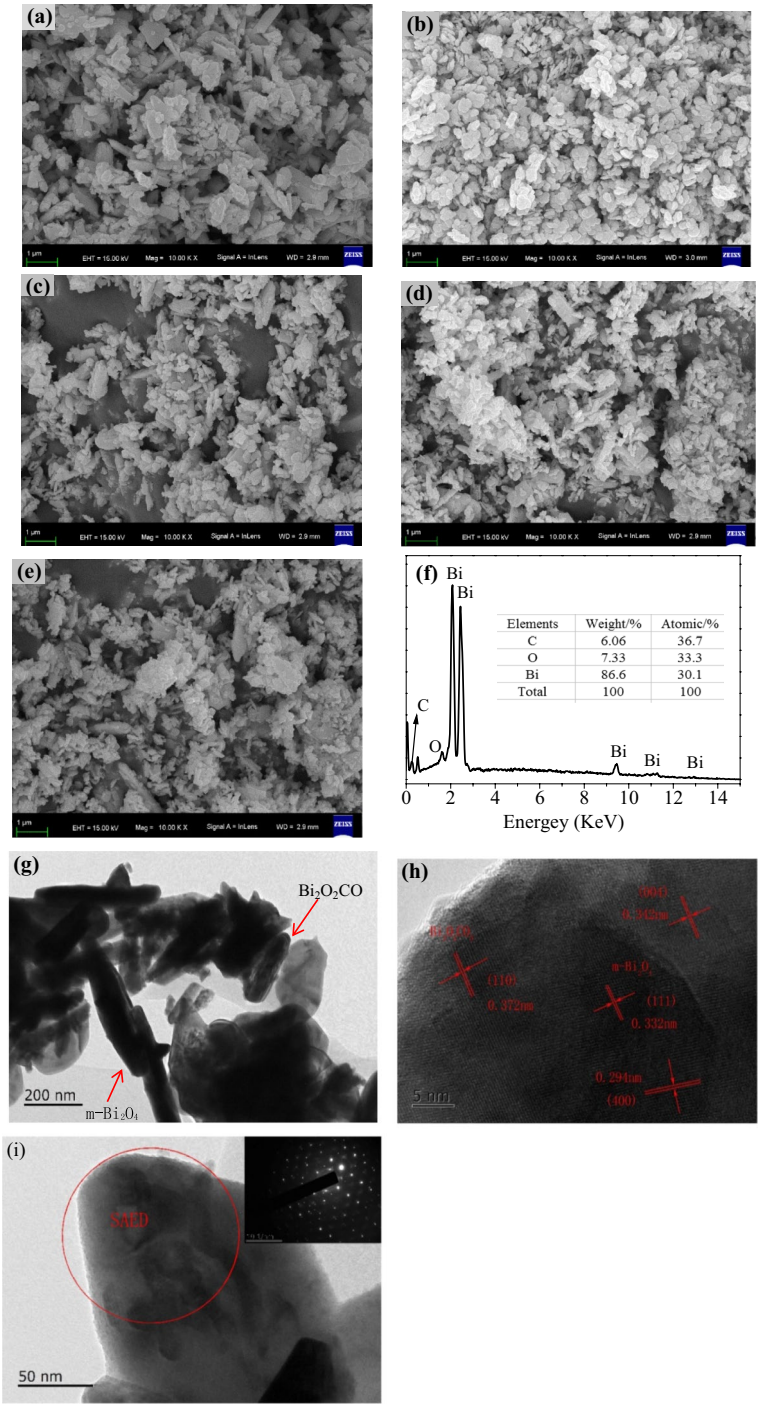

Fig. 4 SEM of m-Bi_2O_4 (**a**), BOC (**b**), 3-B/BOC (**c**), 6-B/BOC (**d**) and 8-B/BOC (**e**), EDS (**f**), TEM (**g**), HR-TEM (**h**) and SAED (**i**) of 6-B/BOC

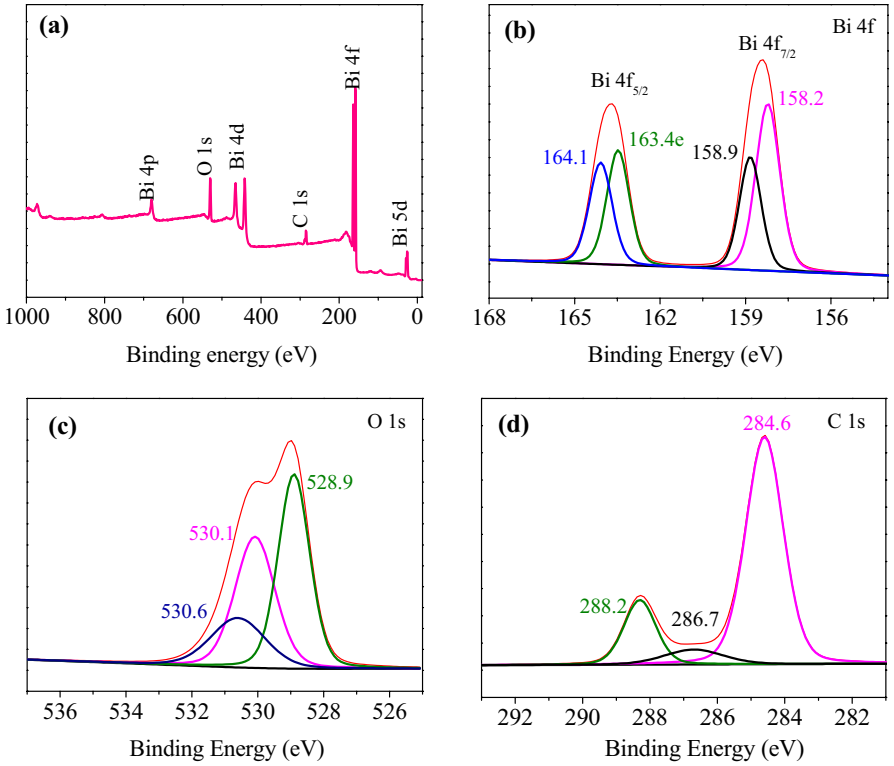

Fig. 5 XPS spectra of 6-B/BOC catalyst: **a** survey spectra, **b** Bi 4f, **c** O 1 s, **d** C 1 s

UV–Vis DRS analysis

The UV–Vis DRS spectrum was utilized to detect the optical performance of the photocatalyst. Based on the data in Fig. 6a, compared to the pure BOC, the absorption wavelengths of m-Bi_2O_4/$Bi_2O_2CO_3$ composites had an obvious red-shift and extended from 363 to 688 nm with the increase of m-Bi_2O_4 content. The results suggested that the UV–Vis absorption properties of m-Bi_2O_4/$Bi_2O_2CO_3$ were impacted, and the intermolecular interaction occurred between m-Bi_2O_4 and BOC, hence the band gap energies of composite photocatalysts were decreased [50].

The band gap energies (E_g) of semiconductors were calculated through the following equations according to the DRS data:

$$\alpha h\nu = A\left(h\nu - E_g\right)^{n/2} \tag{1}$$

and here α, h, ν, and A are the absorption coefficient, Planck constant, light frequency and constant, separately. The value of n is related to the type of transition [51–54]. For m-Bi_2O_4 and BOC, the n values were both 4, indicating an indirect

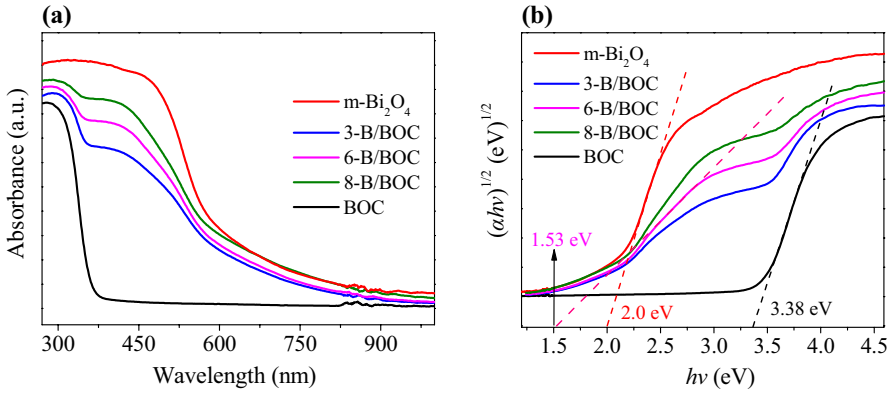

Fig. 6 UV–Vis spectra (**a**) and band gap energies (**b**)

transition. The Tauc plots $[(\alpha h\nu)^{1/2}$ vs. $h\nu]$ were calculated to investigate E_g values. The results are shown in Fig. 6b, and the band gap energies were estimated to be approximately 3.38, 2.0 and 1.53 eV for BOC, m-Bi_2O_4 and 6-B/BOC, respectively.

The potentials of the VB and conduction band (CB) of photocatalysts play a key role on photocatalysis. The VB and CB of semiconductors were calculated based on the following empirical equations:

$$E_{VB} = X - E^e + 0.5E_g \tag{2}$$

$$E_{CB} = E_{VB} - E_g \tag{3}$$

and here X is the electronegativity of semiconductor and E^e is free electron energy (about 4.5 eV vs. NHE). E_g is band gap energy, which has a notable influence on the moving pathway of the photo-generated carriers _ENREF_37 [55, 56]. Based on previous literature, the X value of BOC was 6.36 eV [57, 58] and the VB values were 3.55 and 1.63 eV for BOC and m-Bi_2O_4, respectively. Correspondingly, their CB values were calculated to be 0.17 and − 0.37 eV.

Photocatalytic performance

Photocatalytic performance of the obtained photocatalysts was evaluated through a series of degradation experiments under visible light irradiation using RhB dye as a typical pollutant. The degradation results are presented in Fig. 7. Blank experiments (without catalysts) showed that the performance of RhB was stable and almost no degradation occurred during the process of photocatalysis under visible light. BOC degraded only a small part of RhB, which may be attributed to the sensitization of BOC catalyst excited by RhB dye and the existence of defective centres such as oxygen vacancies [59, 60].

As the contents of m-Bi_2O_4 increased from 30 to 80%, the activities of m-Bi_2O_4/$Bi_2O_2CO_3$ composites were remarkably enhanced compared to the pure BOC photocatalyst. Excitingly, the composites showed good photocatalytic performance about

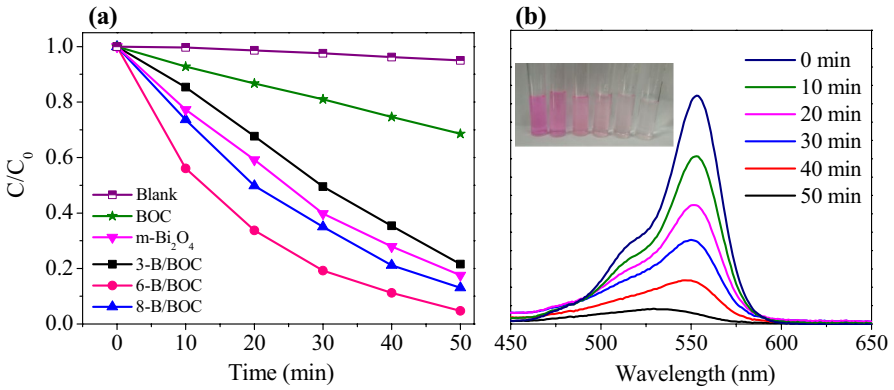

Fig. 7 Photocatalytic degradation of RhB (10 mg/L) under visible light (**a**), the evolution of the spectral changes of RhB with 6-B/BOC as catalyst (50 mg) and a sample obtained every 10 min (**b**)

78.4, 95.3 and 87.0% for 3-B/BOC, 6-B/BOC and 8-B/BOC, respectively. The content of m-Bi_2O_4 in the heterogeneous system affected degradation activities, indicating that the m-Bi_2O_4 could be able to strengthen the absorption to visible light, enhance the separation and transformation of photo-generated carriers and improve the photocatalytic activity [50]. However, the excess content of m-Bi_2O_4 led to a poor degradation, which might be ascribed to the more recombination centres formed by m-Bi_2O_4.

As vividly described in the picture of Fig. 7b, the intensities of peaks decreased and the colour of solution changed gradually from fuchsia to transparent and finally colourless as time went on. Moreover, the maximum absorption wavelength of RhB had a hypsochromic shift from 554 to 530 nm. The movement of maximum absorption peaks for different photocatalysts was further inspected, and the absorption waves shifting with time were tested (not shown).

It was reported that the ethyl groups in the RhB molecule determined the position of the maximum absorption peak. When ethyl groups were destroyed, the position of maximum absorption peak would be changed [61]. Therefore, the above phenomenon might be attributed to the stepwise deethylation and destruction of the conjugated chromophore structure of RhB [16, 62]. The characteristic peak of RhB was still selected as 554 nm in order to simplify the analysis [63].

To quantitatively describe the ability of the photocatalytic reaction, the degradation kinetics of RhB followed a pseudo-first-order equation [50, 64].

$$-\ln\frac{C_t}{C_0} = kt \tag{4}$$

here, k (min^{-1}) is a kinetic constant determined by the plot of the function. All samples were fitted well and had very high correlation coefficients ($R^2 > 0.959$) (Fig. S1, supporting information). The fitted equation, calculated k and correlation coefficient R^2 are listed in Table 1. The calculated values of k were 0.0075, 0.0347, 0.0303,

Table 1 The fitted parameters of photocatalytic degradation for RhB

Catalysts	Fitted equation	k (min^{-1})	R^2
BOC	$y = 0.00745x - 0.00340$	0.0075	0.9976
m-Bi_2O_4	$y = 0.03470x - 0.08114$	0.0347	0.9858
3-B/BOC	$y = 0.03034x - 0.12121$	0.0303	0.9599
6-B/BOC	$y = 0.05909x - 0.04990$	0.0591	0.9898
8-B/BOC	$y = 0.04079x - 0.07949$	0.0408	0.9901

0.0591 and 0.0408 min^{-1} for BOC, m-Bi_2O_4, 3-B/BOC, 6-B/BOC and 8-B/BOC, respectively. These reaction rate constants of 3-B/BOC, 6-B/BOC and 8-B/BOC were about 4.04, 7.88 and 5.44 times higher than that of $Bi_2O_2CO_3$, which demonstrated that the composites showed a quite high ability of photocatalytic degradation for RhB. In addition, the composites of 6-B/BOC had the highest photocatalytic ability. Their excellent photocatalytic activity might be attributed to heterogeneous structure and favorable band gap energy.

To explore the influence factors for degradation of RhB, various concentrations of RhB and a variety of catalyst dosages were investigated. As revealed in Fig. 8a, the degradation of RhB with low concentration was more effective, and high concentration was contrary. Since the additional pollutants adsorbed on the surface of materials under high concentration, the free radicals produced by visible light were overloaded. Furthermore, in Fig. 8b, when the amount of catalysts were increased from 25 to 50 mg, the degradation rate of RhB was remarkably enhanced and increased two times, which confirmed that the more active sites accelerated the degradation rate.

The less the dosage of photocatalysts, the lower the catalytic ability, which was ascribed to the less available active sites. However, excessive dosages would agglomerate, leading to the increase of opacity and light scattering in the system and reducing the surface active sites [65]. Therefore, the degradation efficiency of RhB would be difficult to increase continually.

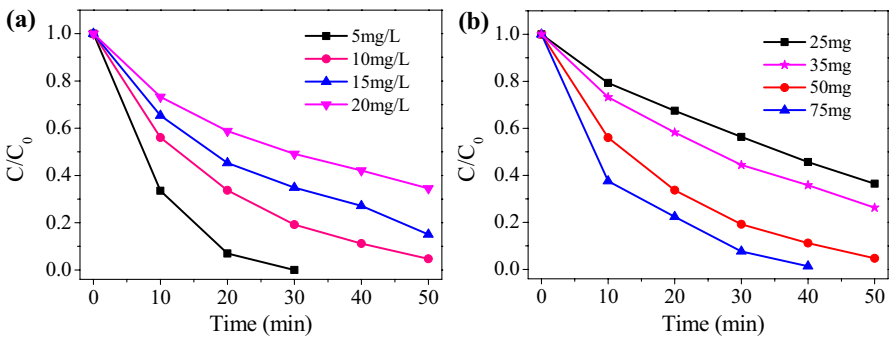

Fig. 8 Factors of photocatalytic degradation reaction: different initial concentrations of RhB (**a**) and a variety of catalyst dosage of 6-B/BOC (**b**)

In general, industrial wastewater contains a variety of dyes. Thence, the degradation performance of 6-B/BOC samples was further investigated for mixed dyes (MO: RhB: MB = 1:1:1, mass ratio). The removal efficiencies of the samples in the darkness were 23.4, 17.8 and 16.7% for MO, RhB and MB, respectively, owing to the too low specific surface area of 12.7 m^2/g of 6-B/BOC. Under visible light, all of the spectral peaks gradually descended and completely disappeared after 50 min (Fig. S2, supporting information). Moreover, the fastest degradation rate of MO might be due to certain selectivity. The results suggested that the as-obtained photocatalyst had a practical application value to treat industrial wastewater.

Photocatalytic mechanism

To explore the mechanism of photocatalytic degradation and evaluate the role of reactive oxygen species (ROS) during the degradation process of RhB under visible light, a series of trapping experiments were implemented with 6-B/BOC samples and different radical scavengers. The scavengers include IPA for •OH, $Na_2C_2O_4$ for h^+ and TEMPOL for $•O_2^-$ [27, 28, 66]._ENREF_22_ENREF_55. As shown in Fig. 9a, it was obvious there was exhibited a lesser degradation of RhB by adding 1 mL of IPA compared to no scavenger. The contribution_ENREF_13 of •OH to_ENREF_56 degradation of RhB was only 9.77%.

The results suggested that •OH played a definite but not the most important role during the degradation process of RhB. On the contrary, while extra $Na_2C_2O_4$ and TEMPOL were put into solution, the noticeable inhibitions were observed, and there was no complete degradation of RhB. The contribution of h^+ and $•O_2^-$ to degradation of RhB were 87.02 and 83.99%, respectively. The values of k for no scavenger, IPA, $Na_2C_2O_4$ and TEMPOL are revealed in Fig. 9b and are 45.77×10^{-3}, 33.4×10^{-3}, 0.67×10^{-3} and 1.39×10^{-3} min^{-1}, respectively. The selective addition of scavengers suggested that h^+ and $•O_2^-$ were dominant active species during the process of photocatalytic degradation. They could directly or indirectly oxidize organics to non-toxic substances.

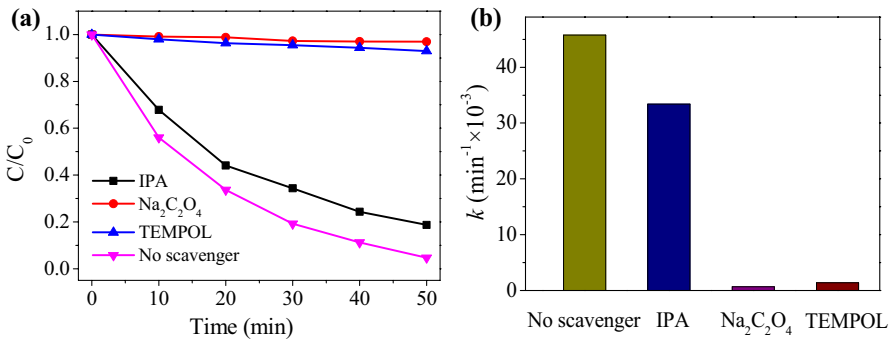

Fig. 9 Photocatalytic degradation RhB (10 mg/L) over 6-B/BOC (50 mg) with a variety of scavengers under visible light (**a**) and the value of the rate constant k with different scavengers (**b**). Dosage of IPA, $Na_2C_2O_4$ and TEMPOL were 1 mL, 25.0 mg and 19.0 mg, respectively

The separation and migration of photo-generated carriers were verified by photocurrent response experiments. The responses were correlated with the separation efficiency of photo-induced e^- and h^+. When the photocatalyst was irradiated under visible light, the strong intensity of the current signal showed a high separation efficiency [67]. According to the mentioned conclusion, the photocurrent property is revealed in Fig. 10.

As forecasted, the photocurrents of these electrodes responded rapidly via light on–off cycles under visible light. Since the large band gap of BOC failed to generated charge carriers, the current signal was poor. The decent photocurrent density of m-Bi_2O_4 was not enough high. However, 6-B/BOC sample exhibited considerably high current density. The above results illustrated that the suitable band structure efficiently separated the carriers and the heterojunction formed by closely contacted interface between two semiconductors was capable of accelerating the movement of photo-generated carriers.

Based on the above test results and calculations, a probable mechanism of photocatalytic degradation of RhB by m-Bi_2O_4/$Bi_2O_2CO_3$ composites was proposed in the following schematic pattern (Fig. 11). Under visible light, m-Bi_2O_4 was excited and produced electron–hole pairs. The electrons on VB were transferred to CB, leaving holes on the VB. However, BOC could not response because of its large band gap. The VB level of m-Bi_2O_4 was not more positive than the standard redox potential of •OH/OH^- (+1.99 eV), thus these holes left on VB could not oxidize OH^- to •OH. Owing to the more positive VB potential of BOC than that of m-Bi_2O_4, the h^+ could only stay on the VB of m-Bi_2O_4 and did not migrate. The accumulated h^+ directly captured organics and then oxidized them.

The electrons on the CB of m-Bi_2O_4 were thermodynamically transferred across the connected interface to the CB of BOC, which was ascribed to the more negative potential of CB for m-Bi_2O_4 than that of BOC. This pattern extended the mobile path and prolonged the electronic lifetime.

In addition, the CB potential of BOC was more negative than the standard redox potential of $E(O_2/\bullet O_2^-, -0.046$ eV), therefore these electrons could react with surface-adsorbed O_2 and reduce them to $\bullet O_2^-$ species. Some $\bullet O_2^-$ also

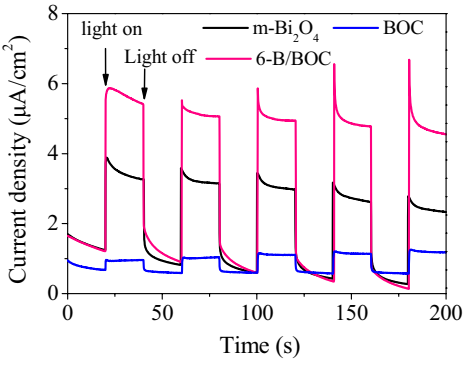

Fig. 10 Photocurrent transient responses for m-Bi_2O_4, 6-B/BOC and BOC

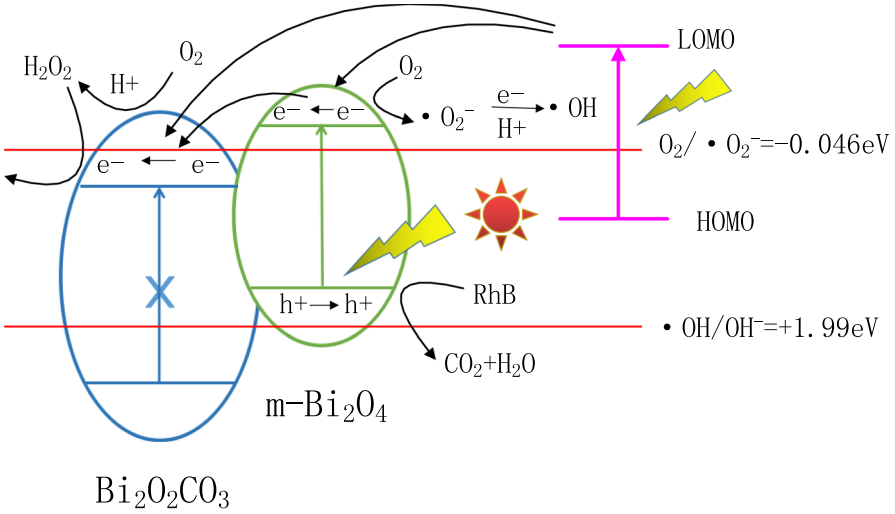

Fig. 11 Schematic diagram illustration for proposed photocatalytic mechanism of m-Bi_2O_4/$Bi_2O_2CO_3$ under visible light

further reacted with e^- and H^+ to generate •OH. Specific reactions were displayed as in the following formulas:

$$O_2 + e^- = \bullet O_2^-, \tag{5}$$

$$\bullet O_2^- + e^- + 2H^+ = H_2O_2, \tag{6}$$

$$H_2O_2 + e^- = \bullet OH + OH^-. \tag{7}$$

The potential of CB for BOC was more positive than $E(O_2/\bullet O_2^-)$ but more negative than the reaction potential of $E(e^-_{CB} + O_2 + H^+ \rightarrow H_2O_2, +0.69$ eV). Hence, the e^- can react with O_2 and H^+ to produce H_2O_2 that can be further reduced to •OH and OH^- [49].

According to previous reports [53, 68], dye molecules were excited and photo-generated electrons transferred from the highest occupied molecular orbitals (HOMO) to the lowest unoccupied molecular orbitals (LUMO), producing singlet and triplet excited states (RhB*)._ENREF_40 Since the potential of LOMO was more negative than that of CB in m-Bi_2O_4 and BOC, the e^- injection from RhB dye to the CB in m-Bi_2O_4 and BOC was feasible, resulting in a high photodegradation of RhB.

All in all, photo-induced electrons and holes were efficiently separated via the connected interface of m-Bi_2O_4/$Bi_2O_2CO_3$ and active species enhanced photocatalytic ability through a series of redox reactions.

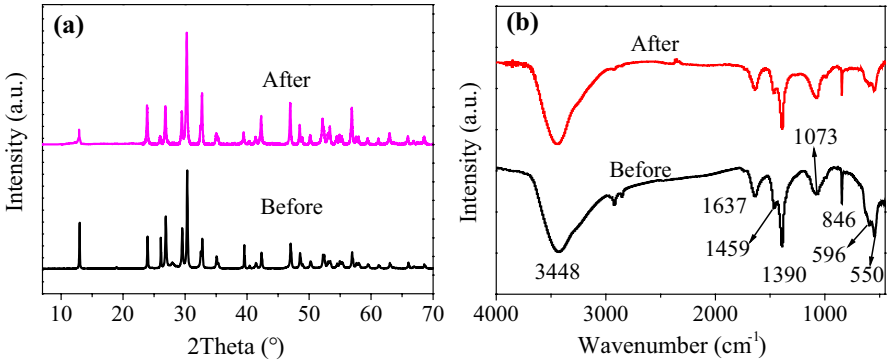

Fig. 12 XRD (**a**) and FT-IR (**b**) patterns of 6-B/BOC before and after photocatalytic reaction

Stability of photocatalysts

The used sample 6-B/BOC was centrifuged, washed with water and ethanol for several times and then dried in a vacuum oven at 333 K. Figure 12a, b displays the XRD and FT-IR patterns of 6-B/BOC before and after the photocatalytic reaction. It was clearly shown that there was no remarkable change in peak shape and no addition peaks appeared, demonstrating that the excellent crystal structure and chemical structure of 6-B/BOC. These results revealed that the 6-B/BOC photocatalyst had good stability.

Conclusions

The heterostructured m-Bi_2O_4/$Bi_2O_2CO_3$ photocatalyst was successfully synthetized through a hydrothermal method and systematically characterized by a variety of analytical instruments. It is concluded that the obtained photocatalyst could be induced by visible light, exhibited superior photocatalytic ability and could simultaneously degrade mixed dyes. The photo-generated electron–hole pairs were efficiently separated, producing a low recombination rate. Furthermore, the h^+ and $\bullet O_2^-$ played an important role during the process of degradation. This study offered an insight into the design of a visible-light-driven photocatalyst applied to environmental remediation.

Acknowledgements This work was supported by the National Natural Science Foundation of China (No. 51578354), the Priority Academic Program Development of Jiangsu Higher Education Institutions, Suzhou Science and Technology Bureau (SS201667), Six Talent Peaks Program (2016-JNHB-067) and Qing Lan Project of Jiangsu Province.

References

1. F. Mian, G. Bottaro, M. Rancan, L. Pezzato, V. Gombac, P. Fornasiero, L. Armelao, ACS Omega **2**, 6298 (2017)
2. X. Xiao, S. Tu, M. Lu, H. Zhong, C. Zheng, X. Zuo, J. Nan, Appl. Catal. B-Environ. **198**, 124 (2016)

3. A. Hameed, M. Aslam, I.M.I. Ismail, N. Salah, P. Fornasiero, Appl. Catal. B-Environ. **163**, 444 (2015)
4. A. Hameed, T. Montini, V. Gombac, P. Fornasiero, J. Am. Chem. Soc. **130**, 9658 (2008)
5. W. Raza, M.M. Haque, M. Muneer, T. Harada, M. Matsumura, J. Alloys Compd. **648**, 641 (2015)
6. L. Jing, J. Wang, Y. Qu, Y. Luan, Appl. Surf. Sci. **256**, 657 (2009)
7. O.F. Lopes, K.T.G. Carvalho, A.E. Nogueira, W. Avansi, C. Ribeiro, Appl. Catal. B-Environ. **188**, 87 (2016)
8. X. Qian, D. Yue, Z. Tian, M. Reng, Y. Zhu, M. Kan, T. Zhang, Y. Zhao, Appl. Catal. B-Environ. **193**, 16 (2016)
9. J. Hou, C. Yang, Z. Wang, W. Zhou, S. Jiao, H. Zhu, Appl. Catal. B-Environ. **142**, 504 (2013)
10. A. Hameed, V. Gombac, T. Montini, M. Graziani, P. Fornasiero, Chem. Phys. Lett. **472**, 212 (2009)
11. D. Wu, L. Ye, A. Ho, Y. Yin, P.K. Wong, Catal. Sci. Technol. **7**, 265 (2016)
12. X. Meng, Z. Zhang, J. Mol. Catal. A-Chem. **423**, 533 (2016)
13. Y. Zheng, F. Duan, M. Chen, Y. Xie, J. Mol. Catal. A-Chem. **317**, 34 (2010)
14. J. Zai, F. Cao, N. Liang, K. Yu, Y. Tian, H. Sun, X. Qian, J. Hazard. Mater. **321**, 464 (2017)
15. H. Huang, N. Tian, S. Jin, Y. Zhang, S. Wang, Solid State Sci. **30**, 1 (2014)
16. D. Hu, K. Zhang, Q. Yang, M. Wang, Y. Xi, C. Hu, Appl. Surf. Sci. **316**, 93 (2014)
17. S. Liu, P. Deng, G. Dai, Y. Liang, S. Zhang, Ceram. Int. **42**, 10094 (2016)
18. X. Feng, W. Zhang, Y. Sun, H. Huang, F. Dong, Environ. Sci-Nano **4**, 604 (2017)
19. X. Feng, W. Zhang, H. Deng, Z. Ni, F. Dong, Y. Zhang, J. Hazard. Mater. **322**, 223 (2017)
20. G. Zhu, M. Hojamberdiev, K.I. Katsumata, X. Cai, N. Matsushita, K. Okada, P. Liu, J. Zhou, Mater. Chem. Phys. **142**, 95 (2013)
21. H. Huang, K. Xiao, Y. He, T. Zhang, F. Dong, X. Du, Y. Zhang, Appl. Catal. B-Environ. **199**, 75 (2016)
22. X. Zhang, T. Guo, X. Wang, Y. Wang, C. Fan, H. Zhang, Appl. Catal. B-Environ. **150**, 486 (2014)
23. W. Wang, H. Cheng, B. Huang, X. Lin, X. Qin, X. Zhang, Y. Dai, J. Colloids Interface Sci. **402**, 34 (2013)
24. J. Chen, W. Mei, Q. Huang, N. Chen, C. Lu, H. Zhu, J. Chen, W. Hou, J. Alloys Compd. **688**, 225 (2016)
25. Q. Zhang, B. Xu, S. Yuan, M. Zhang, T. Ohno, Catal. Today **284**, 27 (2017)
26. L. Song, Y. Pang, Y. Zheng, C. Chen, L. Ge, J. Alloys Compd. **710**, 375 (2017)
27. W. Wang, X. Chen, G. Liu, Z. Shen, D. Xia, P.K. Wong, J.C. Yu, Appl. Catal. B-Environ. **176–177**, 444 (2015)
28. D. Xia, I.M. Lo, Water Res. **100**, 393 (2016)
29. D. Xia, W. Wang, R. Yin, Z. Jiang, T. An, G. Li, H. Zhao, P.K. Wong, Appl. Catal. B-Environ. **214**, 23 (2017)
30. M. Long, P. Hu, H. Wu, J. Cai, B. Tan, B. Zhou, Appl. Catal. B-Environ. **184**, 20 (2016)
31. L. Chen, R. Huang, S. Yin, S. Luo, C. Au, Chem. Eng. J. **193–194**, 123 (2012)
32. Y. Guo, J. Deng, J. Zhu, C. Zhou, C. Zhou, X. Zhou, R. Bai, RSC Adv. **6**, 39762 (2016)
33. Y. Guo, Z. Wang, X. Zhou, R. Bai, Res. Chem. Intermed. **43**, 2273 (2017)
34. Q. Wang, L. Zheng, Y. Chen, J. Fan, H. Huang, B. Su, J. Alloys Compd. **637**, 127 (2015)
35. X.A. Dong, W. Zhang, W. Cui, Y. Sun, H. Huang, Z. Wu, F. Dong, Catal. Sci. Technol. **7**, 1324 (2017)
36. S. Lin, W. Cui, X. Li, H. Sui, Z. Zhang, Catal. Today **297**, 237 (2017)
37. P. Wang, L. Xu, Y. Ao, C. Wang, J. Colloids Interface Sci. **495**, 122 (2017)
38. X. Zhang, S. Li, S. Hu, J. Chen, W. Jiang, J. Zhang, L. Ji, L. Cai, Y. Wang, W. Song, J. Liu, Mater. Lett. **185**, 50 (2016)
39. G. Cai, L. Xu, B. Wei, J. Che, H. Gao, W. Sun, Mater. Lett. **120**, 1 (2014)
40. H. Cheng, B. Huang, K. Yang, Z. Wang, X. Qin, X. Zhang, Y. Dai, Chem. Phys. Chem. **11**, 2167 (2010)
41. Y. Huang, W. Fan, B. Long, H. Li, F. Zhao, Z. Liu, Y. Tong, H. Ji, Appl. Catal. B-Environ. **185**, 68 (2016)
42. H. Lu, L. Xu, B. Wei, M. Zhang, H. Gao, W. Sun, Appl. Surf. Sci. **303**, 360 (2014)
43. Y. Zhou, Z. Zhao, F. Wang, K. Cao, D.E. Doronkin, F. Dong, J.D. Grunwaldt, J. Hazard. Mater. **307**, 163 (2016)
44. Y. Liu, P. Zhang, H. Lv, G. Jing, S. Li, J. Jiang, Rsc Adv. **5**, 83764 (2015)
45. H.Y. Wang, Z.S. Liu, Y.L. Zhao, J.N. Niu, P.Z. Feng, Res. Bull **89**, 253 (2017)
46. C. Yu, W. Zhou, L. Zhu, G. Li, K. Yang, R. Jin, Appl. Catal. B-Environ. **184**, 1 (2016)

47. Y. Ding, G. Zhang, X. Wang, L. Zhu, H. Tang, Appl. Catal. B-Environ. **202**, 528 (2017)
48. T. Xiong, M. Wen, F. Dong, J. Yu, L. Han, B. Lei, Y. Zhang, X. Tang, Z. Zang, Appl. Catal. B-Environ. **199**, 87 (2016)
49. M. Sun, S. Li, T. Yan, P. Ji, X. Zhao, K. Yuan, D. Wei, B. Du, J. Hazard. Mater. **333**, 169 (2017)
50. M. Sun, Y. Wang, Y. Shao, Y. He, Q. Zeng, H. Liang, T. Yan, B. Du, J. Colloids Interface Sci. **501**, 123 (2017)
51. C. Wang, X. Zhang, H. Qiu, W. Wang, G. Huang, J. Jiang, H. Yu, Appl. Catal. B-Environ. **200**, 659 (2017)
52. X. Jin, L. Ye, H. Wang, Y. Su, H. Xie, Z. Zhong, H. Zhang, Appl. Catal. B-Environ. **165**, 668 (2015)
53. N. Guo, Y. Cao, Y. Rong, D. Jia, RSC Adv. **6**, 106046 (2016)
54. A. Hameed, V. Gombac, T. Montini, L. Felisari, P. Fornasiero, Chem. Phys. Lett. **483**, 254 (2009)
55. Z. Wang, Y. Huang, W. Ho, J. Cao, Z. Shen, S.C. Lee, Appl. Catal. B-Environ. **199**, 123 (2016)
56. Y. Bai, L. Ye, T. Chen, P. Wang, L. Wang, X. Shi, P.K. Wong, Appl. Catal. B-Environ. **203**, 633 (2017)
57. W. Shan, Y. Hu, Z. Bai, M. Zheng, C. Wei, Appl. Catal. B-Environ. **188**, 1 (2016)
58. T. Li, X. Hu, C. Liu, C. Tang, X. Wang, S. Luo, J. Mol. Catal. A-Chem. **425**, 124 (2016)
59. Y. Ma, Y. Bian, P. Tan, Y. Shang, Y. Liu, L. Wu, A. Zhu, W. Liu, X. Xiong, J. Pan, J. Colloids Interface Sci. **497**, 144 (2017)
60. M. Sun, Q. Zhao, C. Du, Z. Liu, RSC Adv. **5**, 22740 (2015)
61. S. Shi, M.A. Gondal, A.A. Al-Saadi, R. Fajgar, J. Kupcik, X. Chang, K. Shen, Q. Xu, Z.S. Seddigi, J. Colloids Interface Sci. **416**, 212 (2014)
62. W. Zhao, Y. Wang, A. Wang, J. Qian, W. Zhu, S. Dou, Q. Wang, Q. Zhong, A. Chen, RSC Adv. **7**, 7658 (2017)
63. F. Chang, J. Luo, X. Wang, Y. Xie, B. Deng, X. Hu, J. Colloids Interface Sci. **459**, 136 (2015)
64. G. He, C. Xing, X. Xiao, R. Hu, X. Zuo, J. Nan, Appl. Catal. B-Environ. **170–171**, 1 (2015)
65. R. Hu, X. Xiao, S. Tu, X. Zuo, J. Nan, Appl. Catal. B-Environ. **163**, 510 (2015)
66. H. Huang, K. Xiao, N. Tian, X. Du, Y. Zhang, Colloids Surf. A **511**, 64 (2016)
67. C. Bi, J. Cao, H. Lina, Y. Wang, S. Chen, Appl. Catal. B-Environ. **195**, 132 (2016)
68. X. Chang, M.A. Gondal, A.A. Al-Saadi, M.A. Ali, H. Shen, Q. Zhou, J. Zhang, M. Du, Y. Liu, G. Ji, J. Colloids Interface Sci. **377**, 291 (2011)